Monthly Notices
of the
ROYAL ASTRONOMICAL SOCIETY

MNRAS **509,** 6169–6178 (2022)
Advance Access publication 2021 December 2

https://doi.org/10.1093/mnras/stab3470

Realistic energy deposition and temperature heating in molecular clouds due to cosmic rays: a computation simulation with the GEANT4 code employing light particles and medium-mass and heavy ions

Sergio Pilling,[1]★ Maurício Tizziani Pazianotto,[2] Lucas Alves de Souza[2]
and Larissa Maciel do Nascimento[1]

[1]*Instituto de Pesquisa & Desenvolvimento (IP&D), Universidade do Vale do Paraíba (UNIVAP), São Jose dos Campos 12244-00, Brazil*
[2]*Instituto Tecnológico de Aeronáutica (ITA), São Jose dos Campos 12228-900, Brazil*

Accepted 2021 November 25. Received 2021 November 25; in original form 2021 October 26

ABSTRACT

In the interstellar medium, Galactic and extragalactic cosmic rays (CRs) penetrate deeper in the molecular clouds (MCs) and promote inside several physical and physicochemical changes due to the energy deposition, including gas and grain heating, and triggering also molecular destruction and formation. In this work, in an attempt to simulate, in a more realistic way, the energy delivered by CRs in a typical MC (mass $\sim$5400 $M_\odot$ and size $\sim 10^6$ au; mainly composed of H atoms), we combine the energy deposition of light particles and heavy ions, with the new calculations considering the medium-mass ions ($3 \leq Z \leq 11$). To execute the calculation, the Monte Carlo toolkit GEANT4 was applied to get the energy deposition rate per mass from many kinds of secondary particles, used in nuclear and hadron physics. The energy deposition by its induced cascade shower within the MC was characterized, as well as the relative energy deposition for all members of the medium-mass group. The results show that the incoming protons are the dominant source in the energy deposition and heating of the cloud, followed by alphas and electrons, with the medium-mass-ion and heavy-ion groups each contributing roughly 8 per cent. The current model also shows a temperature enhancement of up to 10 per cent in the external layers of the cloud (reaching 22.5 K) with respect to the previous calculations where only light particles were considered. However, neither heavy nor medium-mass ions contribute to the temperature enhancement in the deep core of the cloud.

Key words: astrochemistry – astroparticle physics – atomic processes – software: simulations – ISM: clouds – cosmic rays.

1 INTRODUCTION

Cosmic rays (CRs) are an important agent for atom/molecular ionization and heating in molecular clouds (MCs). In the darker clouds or in the deeper regions of MCs, also named dense cores, which are shielded from the external UV radiation field, they are the only source of heating (Goldsmith & Langer 1978; Galli & Padovani 2015). As discussed by Pazianotto et al. (2021, hereafter Paper I) and references therein, the irradiation of MCs by CRs provokes several physical and physicochemical modifications, which include the addition of energy that heats up the system and the generation of particles (intranuclear cascade) up to molecular destruction and finally the creation of new species. During the interaction, all the particles that were assembled (i.e. secondary protons, neutrons, pions, muons, photons, electrons, etc.) interact with the medium through several processes, giving off some of their energy directly and indirectly.

It has been a huge challenge to comprehend the energy deposition in distinct regions of an MC for different CR-induced particles and their impacts on the heat balance in the cloud. For example, the effects of the most abundant ions, such as protons, alphas, and electrons (named the group of light particles), on the energy deposition within MCs were simulated in Paper I. Later on, Pilling et al. (2021, hereafter Paper II) made an extension of this work and computed the energy deposition due to iron ions as well as all the combined ions within the heavy-ion groups ($12 \leq Z \leq 29$), indicating that the contribution of heavy ions in the energy deposition is low ($\sim$10 per cent in outer layers and $\sim$0 per cent in the centre). In this paper, to simulate in a more realistic way the energy deposition and temperature heating in an MC due to CRs, we performed a novel computation simulation considering ions with broader atomic numbers, with $1 \leq Z \leq 29$ (which includes the medium-mass ion group and the values obtained in the previous calculations for light and heavy particles), as well as the electronic component of CRs. The methodology here is similar to that of the previous papers (Paper I and Paper II) but the types of input CRs are different. Once more, the energy flux distribution was taken from the measurements of *Voyager I* in the interstellar medium (ISM) published by Cummings et al. (2016).

In order to execute the calculation, the Monte Carlo toolkit GEANT4 (Agostinelli et al. 2003; Allison et al. 2006) was applied to get the energy deposition rate per mass from many kinds of secondary particles, along the MC, and its energy spread within the cloud. All the reactions from the nuclear data library and the scattering process for several types of particles were considered. The importance of determining the energy deposition within the

★ E-mail: sergiopilling@yahoo.com.br

cloud is that it can be used to estimate the cloud's heating (and therefore the cloud's temperature profile). Since the temperature influences chemical reactions, the incoming CRs, as well as their secondary particles, also affect the chemical balance of the medium, also modulating the chemical profiles within the MC.

In the literature, the related theoretical studies use varied methodologies for MC analysis. For example, the translational energy dissipation and desorption rate were studied by adding equation variables to model the effect (Fedron et al. 2021). Grudić et al. (2019) employed another verified technique for MC analysis, which includes the use of magnetohydrodynamics (MHD) simulations in order to report feedback with respect to intrinsic or observational scattering. Additionally, several simulations are used for CR and MC analysis; among them, we highlight the work of Hopkins et al. (2020), who used in their study simulations with the multiphysics code GIZMO, based on the Lagrangian method, which provides accuracy through the methods used by MHD. Finally, according to Grassi et al. (2019), the simulations that check parameters such as magnetic field and CR density and relate them to temperature-dependent chemistry imply targeting coefficients that indicate a reaction rate of CR ionization.

In the last 10 years, numerous experiments employing swift medium-mass ions, with energies from tens of kiloelectron volts to hundreds of megaelectron volts, on ices or/and solid grains have shown that such projectiles indeed produce chemical changes in the samples and contribute to enhancing the molecular complexity in materials in space environments (e.g. Pilling et al. 2011, 2012; Ly et al. 2012; de Barros et al. 2014; Boduch et al. 2015; Vasconcelos et al. 2017a,b,c; Rachid et al. 2020) A comparison between the effects of medium-mass ions and those of other incoming ionizing radiation in ices was also performed. In one of these works, Vasconcelos et al. (2017b) pointed out that for H_2:CH_4 ices irradiated at 19 K by 15.7 MeV O ions, the effective destruction yield (in molecules/impact) of the parental species processed by the swift ions can reach up to six orders of magnitude higher than the value determined by employing soft X-rays, which indicates once more that inside obscured MCs these charged projectiles are very important to drive the chemistry and the heating processes.

It is important to highlight also the laboratory studies that investigate CRs describing their particularities related to atmospheric phenomena on Earth, such as the ones described by the Carpet detector that monitors the intensity of secondary CRs since 2006 in the El Leoncito Astronomical Complex, showing the importance of CR variations using temperature variation methods (De Mendonça et al. 2013). According to Loewenstein, Zweibel & Begelman (1991), the production of temperature gradients generates models that help in setting up the analysis of CR transformation models, which can be obtained by thermal pressure. Some analysis methodologies involve empirical methods, such as the one that uses muon detectors from the Belgrade CR station based on the ground and subsurface affected by atmospheric parameters (Savić et al. 2019).

This paper is divided as follows: In Section 2, we introduce the computational methodology used in this work using the GEANT4 code, as well as some information about the integrated energy flux of the employed ion sources. In Section 3, the principal outcomes are discussed, with focus on the energy provided by each particle in the cascade particle inventory along the collisions inside the cloud, the overall energy taken within the cloud by the incoming CRs, and the outcomes for a first-order model for the temperature enhancement inside the MC due to energy delivered by CRs. Additionally, an analysis correlating the astrophysical works through bibliographic research is presented. Finally, the summary and conclusions are provided in Section 4.

2 METHODOLOGY

The simulation of the interaction between ionizing particles (CR analogues) with matter has been performed to allow the understanding of energy delivered within MCs and also gas heating. First, the effects of the most abundant ions, such as protons, alphas, and electrons (named the group of light particles) on the energy deposition were considered (Paper I). Second, we compute the energy deposition due to iron ions, as well as all the combined ions within the heavy-ion groups ($12 \leq Z \leq 29$) (Paper II). This second work shows that the total energy deposition due to the heavy-ion group was only roughly 10 per cent higher (outer layers) and virtually the same at the centre of the cloud when compared with the previous model (only considering light particles). Both simulations have been performed employing the Monte Carlo code GEANT4 (Agostinelli et al. 2003; Allison et al. 2006; GEANT4 Collaboration 2012).

In the current work, to simulate in a more realistic way the energy delivered by CRs in a typical MC, we add to the previous calculations the effect of the medium-mass group ($3 \leq Z \leq 11$). First, we calculate, in detail, the energy deposition rate during the transport of carbon ions throughout the MC considering also their cascade particles and their energies delivered. Such a procedure was also performed for the other incoming sources (light particles and iron ions). The geometry and composition of the MC and also the incidence and analysis methodology can be found in Paper I and Paper II.

The parametrization to simulate the hadronic interactions was performed with the QGSP_INCLXX_HP reference physics list. This physics list is the same as that employed in the previous simulations of the effects of CR protons, alphas, and electrons on an MC. Once more, the simulation was performed considering a spherical MC with 5400 solar masses with a radius of around 1×10 au, with a density higher in the centre, and divided into 13 concentric shells with parameters and energy deposition in each shell described by the average quantities within the shell. The other parameters considered for the simulated object are the density profile law of $r^{-1.2}$ and average number density of 200 cm^{-3} containing mostly H atoms (with also C atoms as a minor component to represent dust grains), with the canonical dust-to-gas ratio of 1/100 (more details in Paper I).

As employed in Paper I and Paper II, here, once more, we consider the realistic CR fluxes taken from the measurements of *Voyager I* in the ISM published by Cummings et al. (2016). We observe that for energies below $\sim 1 \times 10^4$ MeV the integrated flux of CRs is dominated by lighter particles. For energies above $\sim 10^5$ MeV, the integrated flux of all nuclei components is comparable. For comparison purposes, the primary fluence rates (integrated from $\sim 10^{-1}$ to 10^6 MeV) that we have obtained for the simulations are 1.26 protons $cm^{-2}\ s^{-1}\ sr^{-1}$, 0.09 alphas $cm^{-2}\ s^{-1}\ sr^{-1}$, 1.19 electrons $cm^{-2}\ s^{-1}\ sr^{-1}$, 2.30×10^{-3} carbons $cm^{-2}\ s^{-1}\ sr^{-1}$, and $1.81 \times 10^{--4}$ irons $cm^{-2}\ s^{-1}\ sr^{-1}$. The total particles considered in each group were 2.54 light particles $cm^{-2}\ s^{-1}\ sr^{-1}$, 6.39×10^{-3} medium-mass ions $cm^{-2}\ s^{-1}\ sr^{-1}$, and 1.20×10^{-3} heavy ions $cm^{-2}\ s^{-1}\ sr^{-1}$. All the simulations were performed in order to obtain uncertainty below 10 per cent.

3 RESULTS AND DISCUSSION

The outcomes for the calculations using the more realistic incoming CR field in a typical MC are shown in the following subsections. In Section 3.1, we point out the calculated deposited energy in the MC for the many components in the cascade shower due to the distinct primary particle spectra used in this work (with the integrated flux measured by *Voyager I*). This section also presents the total energy deposited by each ion group considered (light particles,

medium-mass ions, and heavy ions). In Section 3.2, the temperature in each layer of the simulated MC in a steady-state situation is figured out, taking into account the balance heat applying the current data of energy deposition and the methodology described by Goldsmith (2001).

3.1 Energy provided by CRs

The energy delivered by each particle within the cascade particle (e.g. depending on the case, the primary protons, alphas, electrons, irons, and carbons, and the secondary protons, alphas, electrons, positrons, photons, neutrons, deuterons, tritions, pions+, pions−, muons+, and muons−) for the several considered CR sources is shown in Fig. 1. As discussed previously, the realistic CR flux data from *Voyager I* measured at the ISM (taken from Cummings et al. 2016) were considered.

Figs 1(a)–(c) present the results for the lighter sources, protons (the most dominant agent), alphas, and electrons, respectively. In Fig. 1(a), we show the cascade particle energy deposition when the proton source is considered. As expected here, the protons are the main source of energy deposition, followed by their induced secondary electrons and positrons. Curiously, the secondary alphas, deuterons, and tritions virtually do not deposit energy in the layers between 100 and 1000 au from the centre. With the exception of protons and secondary electrons, all the other particle cascades deposit more energy in the central regions than the outer regions. Fig. 1(b) shows the cascade particle energy deposition when the alpha source is considered. After the alphas, the secondary electrons, protons, deuterons, tritions, and positrons (in this order) respond to the main input of energy in this case.

The cascade particle energy deposition for the electron source is presented in Fig. 1(c). In this figure, besides the electrons, only secondary positrons, photons, and protons contribute actively in the energy deposition. Curiously, in this case, the secondary photons are the second most important cascade particle in the energy deposition at the outer layers of the cloud and secondary positrons are the second most important cascade particle in the energy deposition in the deep core of the cloud. The secondary protons virtually do not deposit energy in the layers between 100 and 3000 au from the centre.

Fig. 1(d) presents the results for the energy deposited by Fe ions, the typical constituent of the heavy-ion group, and its cascade particles in the MC (additional details can be obtained in Paper I). After the Fe ions, the second most important agent in the energy deposition was the secondary electrons, both depositing more energy in the cloud's outer layers. The secondary protons, alphas, and deuterons are other indispensable agents in the energy deposition, depositing more energy in the centre than in the outer layers of the cloud.

Finally, Fig. 1(e) shows the results for the energy deposited by C ions, the typical constituent of the medium-mass group. In this panel, we observe, as expected, that carbon ions represent the most important component here, followed by secondary electrons, alphas, protons, deuterons, and the others. The energy deposition of carbon and the secondary electrons has a maximum in the outer layers of the cloud. For the other particles, we observe the contrary behaviour (the maximum energy deposition occurs in the deep centre of the cloud). It is worth noting that in all the panels of Fig. 1 the secondary photons (mainly gamma) have an energy deposition that varies little with the distance to the centre (i.e. the secondary photons have the lowest gradient in the energy deposition of the cascade particles). Future studies will focus on the energy distribution of these secondary photons inside the MCs due to the incoming CR.

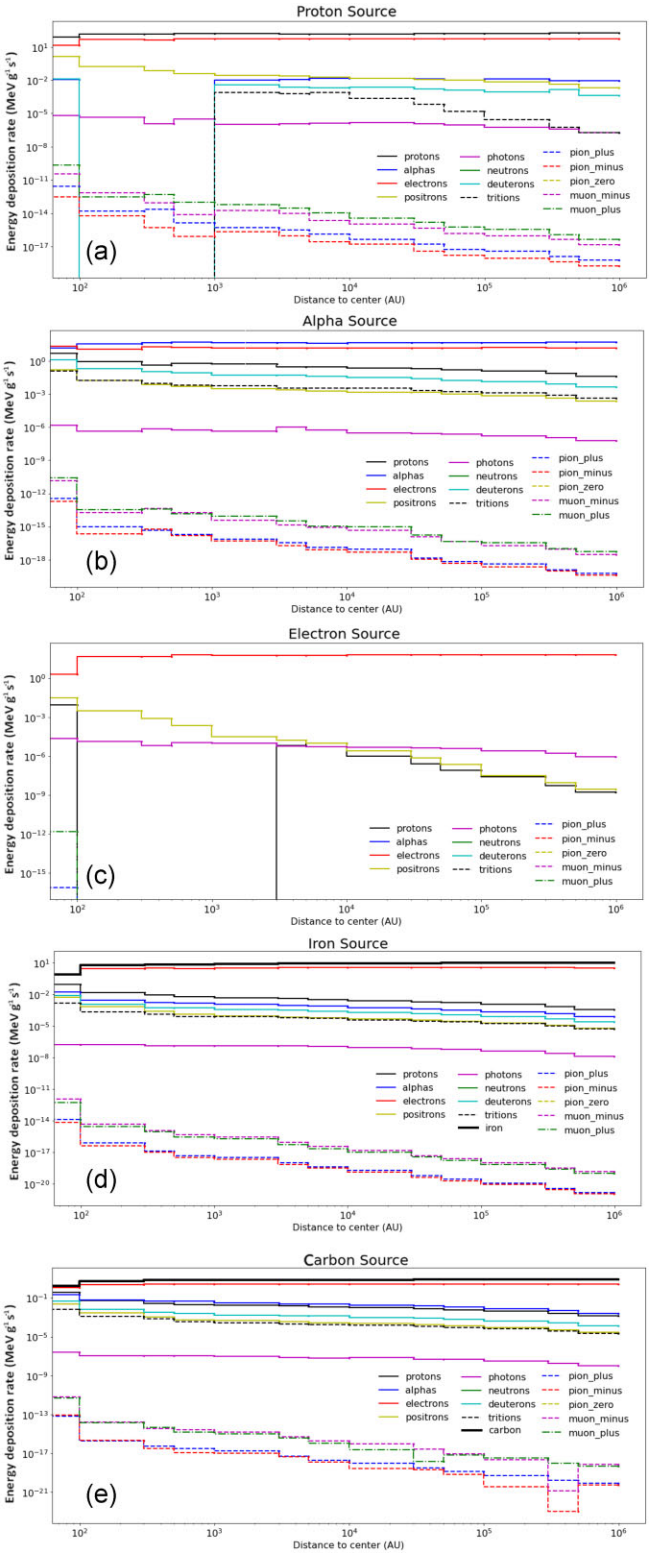

Figure 1. Energy deposition rate by the different components of the cascade shower during collisions of (a–c) light sources (protons, alphas, and electrons), (d) iron source (a typical constituent of the heavy-ion group), and (e) carbon source (a typical constituent of the medium-mass group) in the simulated MC considering the CR flux data from *Voyager I* measured at the ISM. See details in the text.

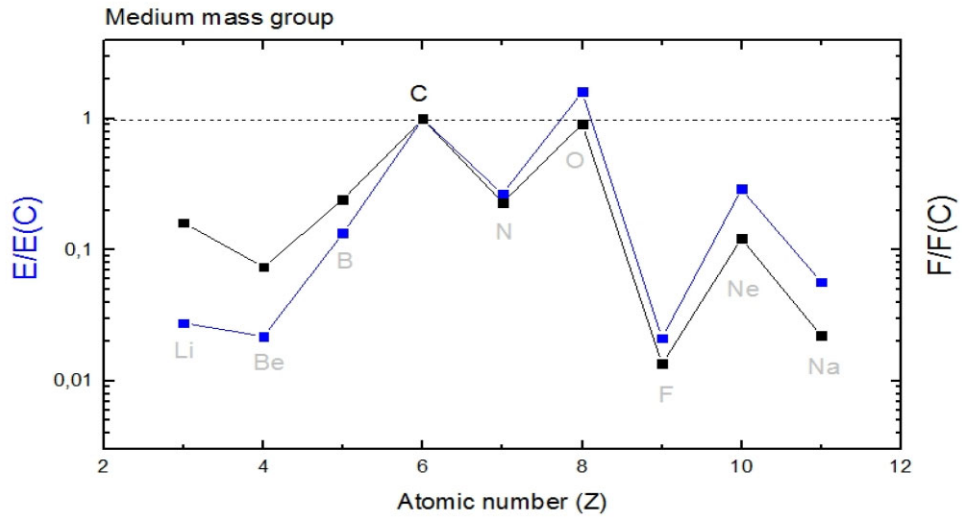

Figure 2. Comparison between the deposited energy and the integrated flux of the ions within the medium-mass group ($3 \leq Z \leq 11$) with respect to the carbon. Simulations were performed considering more than 99.99 per cent of the MC's volume and mass (up to the ninth innermost layer). The integrated flux was taken from Cummings et al. (2016).

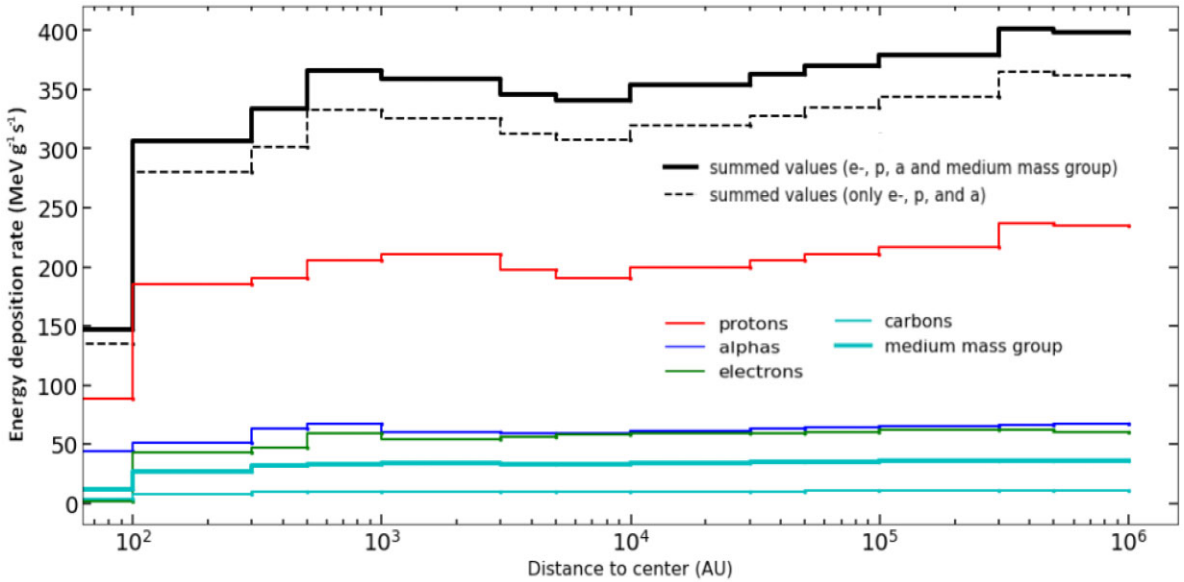

Figure 3. Energy deposition rate for each primary source [protons, alphas, and electrons (from Paper I)], carbon, and the medium-mass group (this work)) in the simulated MC.

Fig. 2 presents a comparison between the deposited energy rate and the integrated flux of the ions within the medium-mass ion group with respect to the carbon. For the calculation of the energy deposition ratio (presented in blue), we consider the effect up to the ninth inner layer within the cloud (which corresponds to more than 99.99 per cent of the cloud volume and mass). In terms of integrated flux (presented in black colour), the C ions are the dominant agent in this group, followed by O, B, and N ions. Curiously, in terms of the deposited energy (presented in blue colour), the O ions are dominant, followed by C, Ne, and N. Within this medium-mass group, F is the ion with the lower value for both the integrated flux and the energy deposition rate. These individual differences were taken into consideration in the calculation of the total energy delivered by the medium-mass ion group.

Fig. 3 presents the total energy deposition rate, in units of megaelectron volts per gram per second, for the primary sources of protons, alphas, electrons, and carbon, as well as the medium-mass group considered as a whole (considering the energy and flux distribution shown in Fig. 2). The solid black line shows summed values obtained in the current simulation (electrons + protons + alphas + medium-mass ion sources). The dashed line shows only the summed values, considering only the light particles (Paper I) for comparison purposes. The energy deposition rate for the C source is given by the light cyan curve, and for the medium-mass group by the bold cyan curve. We observe that the current simulation, which considers the effect of medium-mass CRs in the MC, induces a small enhancement in the energy deposition rate with respect to the simulation considering only light particles (being minimal in the deep core of the cloud). Curiously, this same behaviour was observed when only heavy ions were considered in the calculations, as pointed out by Paper I. This reinforces that the major components of the energy delivered inside MCs are

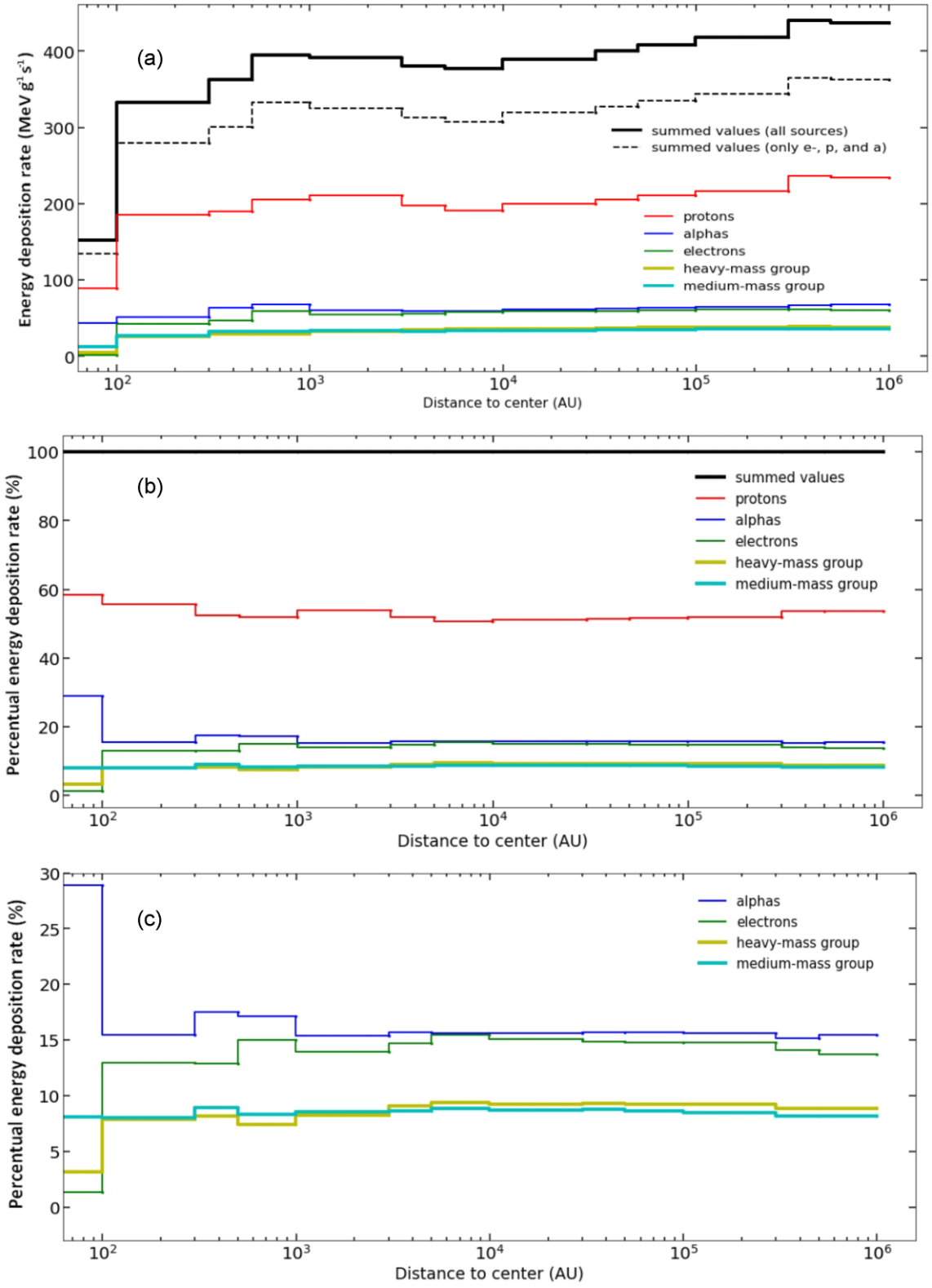

Figure 4. Energy deposition rate of the most realistic incoming radiation field considering light particle sources [protons, alphas, and electrons (from Paper I)], the heavy-mass group source (from Paper II), and the medium-mass group source (this work) in the simulated MC. (a) The energy deposition rate in units of megaelectron volt per gram per second, with the black lines presenting two sets of summed values considered [black dashed line: the CR field with only light particles (Paper I); black bold solid line: the most realistic CR field (this work)]. (b) The energy deposition rate in percentage for the CR sources of protons, alphas, electrons, the medium-mass group, and the heavy-ion group). (c) An amplification of panel (b), showing percentages from 0 to 30 per cent, for better visualization.

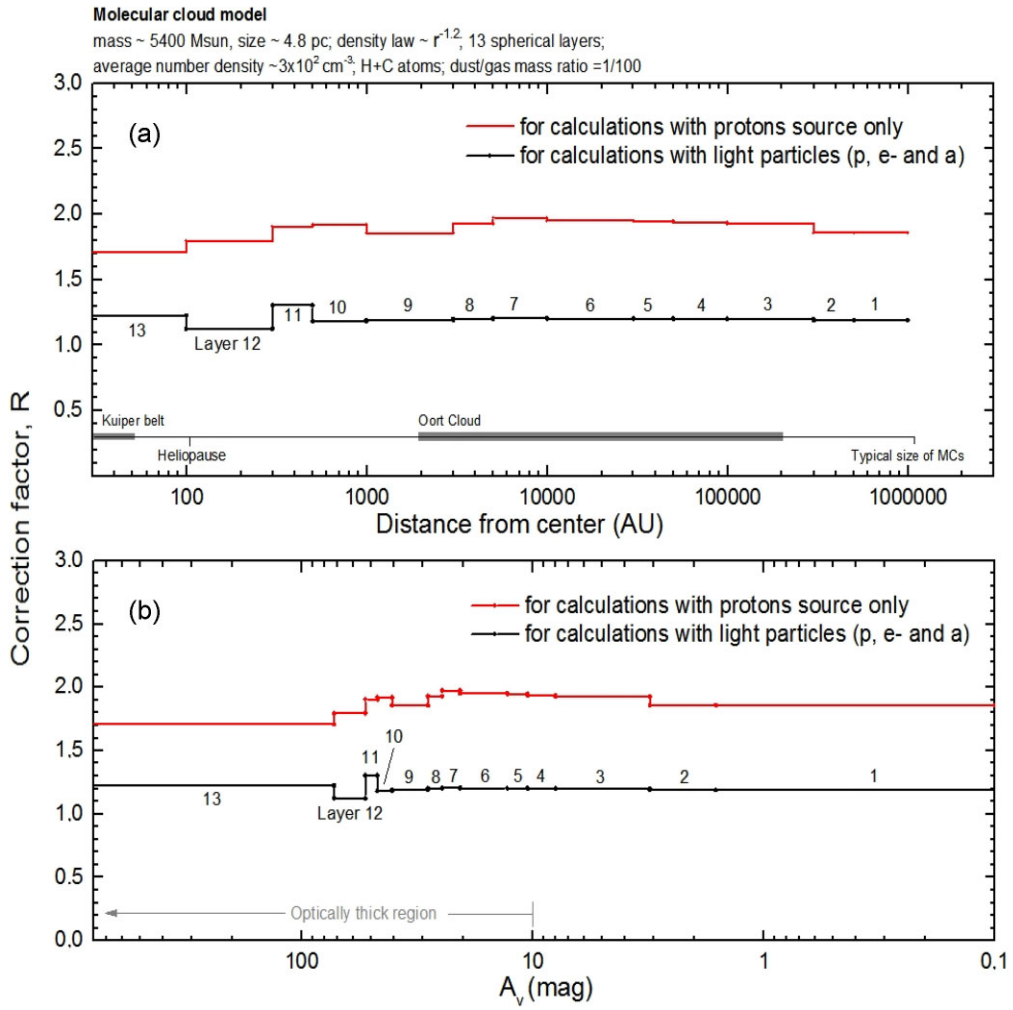

Figure 5. Correction factor for energy deposition rate to simulate the realistic incoming CR field (light particles + medium-mass ions + heavy ions) in comparison with the calculations considering only proton sources (red curve) and light particles (protons + electrons + alphas) (black curve). The correction factor (a) as a function of distance from centre (au) and (b) as a function of visual extinction (mag). The numbers of the layers in the model are indicated by the black labels. Some model parameters are given in the figure header. See details in the text.

indeed protons (major), alphas, and electrons (see also Paper I and Paper II).

The energy deposition rates of the most realistic incoming radiation field considering light particles [(protons, alphas, and electrons (from Paper I)], the heavy-mass group (from Paper II), and the medium-mass group (this work) in the simulated MCs are shown in Fig. 4(a) in units of megaelectron volts per gram per second, with the black lines presenting two sets of summed values considered [black dashed line: the CR field with light particles only (Paper I); black bold solid line: the most realistic CR field (this work)]. The energy deposition rates, in percentage, for the CR sources protons, alphas, electrons, the medium-mass ion group, and the heavy-ion group are given in Fig. 4(b); Fig. 4(c) is an amplification of Fig. 4(b) for better visualization of the differences in the energy deposition rates of the different incoming CR sources. In this figure, we observe some important findings in the individual contribution to the energy deposition rate due to CRs: (i) The proton source (more precisely, all the cascade particles produced by the incoming protons plus the protons themselves) corresponds to roughly 52–59 per cent (with the maximum at the deep core of the cloud, below 100 au); (ii) the maximum contribution of the alpha source (about 29 per cent) is in the deep core; (iii) the contribution of the alpha source is a little higher than the contribution of the electron source, both being around 13–15 per cent from distances between 3×10^3 au up to 3×10^5 au; (iv) the maximum contribution of the electron source is around 0.6–1×10^4 and its minimum contribution (only 3 per cent) is in the deep core; (v) at distances larger than 100 au from the centre, both medium-mass ion group and heavy-ion groups are responsible for roughly 8 per cent each in the energy deposition rate due to the incoming CRs; and (vi) in the deep core the contribution of the heavy-ion group in the energy delivery rate is even lower, only about 3 per cent.

Fig. 5 presents the multiplicative correction factor (R) that can be adopted to transform the named simplistic energy delivery rate (E_s), calculated considering only a proton source (red curve) or considering only light particles (protons + electrons + alphas; black curve), into the realistic energy delivery rate ($E_r = R \times E_s$), which considers a more realistic incoming CR field taking into account light particles, medium-mass ions, and heavy ions. Fig. 5(a) shows the correction factor as a function of the distance from the centre of the cloud, and Fig. 5(b) as a function of visual extinction. The correction factor for calculations employing only a proton source is around

Table 1. Numerical values for the current model during the cloud's temperature (T_{gas}) estimation due to the heating induced by CRs considering a realistic energy deposition (employing light particles, medium-mass ions, and heavy-mass ions). Additional information for T_{dust} and the parameters α and β can be obtained from Goldsmith (2001).

Layer	Outer and inner radii (au)	Deposited cosmic ray energy rate, $G_{gas,cr}$ (MeV g^{-1} s^{-1})	Deposited cosmic ray energy rate, $G_{gas,cr}$ (erg cm^{-3} s^{-1})	Average number density, ρ (g cm^{-3})	Average column density, $n(H_2)$ (cm^{-3})	A_v[a] (mag) at inner radii	α[b] (erg cm^{-3} s^{-1})	β[b]	T_{dust}[c] (K)	T_{gas}[d] (K)
1	9.4e+05–5.0e+05	436.90	4.54e−25	6.50e−22	196.27	1.6	1.2e−25	1.7	6.0	22.5
2	5.0e+05–3.0e+05	440.01	1.05e−24	1.49e−21	450.90	3.1	5.1e−25	2.0	6.1	14.5
3	3.0e+05–1.0e+05	418.01	3.24e−24	4.85e−21	1463.01	7.9	1.4e−24	2.3	6.2	14.4
4	1.0e+05–5.0e+04	408.31	6.73e−24	1.03e−20	3110.65	10.5	2.3e−24	2.5	6.3	15
5	5.0e+04–3.0e+04	400.18	1.51e−23	2.37e−20	7146.33	12.9	4.4e−24	2.7	6.6	15.4
6	3.0e+04–1.0e+04	389.63	4.78e−23	7.68e−20	23 187.14	20.6	1.1e−23	2.9	7.0	15.5
7	1.0e+04–5.0e+03	376.75	9.84e−23	1.63e−19	49 299.49	24.7	1.6e−23	3.0	7.4	15.1
8	5000–3000	380.48	2.28e−22	3.75e−19	113 261.31	28.4	2.3e−23	3.1	7.5	13.4
9	3000–1000	391.49	7.62e−22	1.28e−18	367 477.39	40.7	3.8e−23	3.2	7.6	10.3
10	1000–500	394.93	1.63e−21	2.59e−18	781 356.78	47.1	4.6e−23	3.3	7.6	9.0
11	500–300	363.12	3.45e−21	5.95e−18	1.795e6	53.1	5.5e−23	3.4	7.7	8.3
12	300–100	333.08	1.02e−20	1.93e−17	5.824e6	72.5	6.8e−23	3.7	7.8	8.0
13	100–0	151.95	1.38e−18	5.69e−15	1.721e9	∼2900	1.2e−22	4.7	8.0	8.1

[a]Considering the canonical equation for the visual extinction (A_v), A_v (mag) $= N_H/1.8 \times 10^{21}$ cm^{-2}, where $N_H = 2N_{H_2}$ (Bohlin et al. 1978). For each layer in the model, the N_{H_2} is obtained from the number density (n_{H_2}) times the thickness of the layer.
[b]Considering the gas-cooling function (see Goldsmith 2001).
[c]Considering typical gas–dust coupling and intermediate molecular depletion (from model DF10 of Goldsmith 2001).
[d]Calculated in this work.

1.5–2 (with the maximum correction at A_v ∼20 mag), indicating, once more, that protons correspond with the most part of the energy delivery inside the MC. For the calculation considering only light particles, the correction factor is around 1.2. The employment of this R factor in similar future studies will decrease the computer time needed in the simulations.

3.2 Molecular cloud's temperature estimation

It is known from observations that the MCs' temperatures are very low, roughly 7–15 K (e.g. Pan & Padoan 2009; Dobbs et al. 2014) and that the incoming radiation, mainly the penetrating CRs from the Galactic and extragalactic medium, plays an important role in the heating balance in MCs (e.g. Goldsmith 2001).

The temperature profile of a typical MC (ruled mainly by the gas temperature, T_{gas}) considering only the effect of incoming light CRs (protons + alphas + electrons) was calculated in Paper I, employing a steady-state scenario, and the thermal balance of the gas and dust coupled together by the gas–dust collisions. That calculation was done by solving the thermal equilibrium condition, discussed in detail in Goldsmith (2001). In the current manuscript, we consider a more realistic incoming CR field (containing light particles, medium-mass ions, and heavy ions) and perform a new calculation, for the MC's temperature profile, considering the same methodology as that used previously. The values considered in the current calculation are listed in Table 1. In this table, the temperature of dust inside the cloud (T_{dust}), and the parameters α and β employed in the estimation of the gas cooling function are all dependent on the number density $n(H_2)$, and were calculated considering the equations described by Goldsmith (2001).

Fig. 6 shows the average MC temperature of each layer obtained by the current work considering as energy input a realistic CR field (containing light particles, medium-mass ions, and heavy ions), and also the balance heat equations in a steady-state regime, as discussed by Goldsmith (2001). The red line presents the temperature profile within the cloud using the current CR energy delivery, the blue line shows the calculation employing only light ions (Paper I), and the dashed black line presents the calculation by Goldsmith (2001) (an interpolation from model DF10). Figs 6(a) and (b) present the temperature as a function of the central MC's distance (in units of au) and as a function of the average visual extinction of the layer, respectively. The labels of the MC layers are indicated by numbers. The current model (red line) shows a temperature enhancement of up to 10 per cent in the other layers of the clouds (reaching 22.5 K) with respect to the previous calculations (blue line) when only light particles were considered. The current model also shows that neither heavy nor medium-mass ions contribute to the temperature enhancement in the deep core of the cloud.

The major discrepancies between the two models employing the GEANT4 calculations and the model DF10 of Goldsmith (2001) observed in Fig. 6 happen at two distance ranges: the first between 3×10^3 and 3×10^4 au with the Goldsmith model having a lower gas temperature and the second between 1×10^5 and 5×10^5 au in which the Goldsmith model has a higher gas temperature. It is worth noting that, looking at the temperature profile as a whole, for both models obtained by the GEANT4 calculations, in contrast to the Goldsmith model, we observe a rapid drop in the temperature (roughly 7 K) between layers 1 and 2 (in the outer regions of the cloud) and a small temperature increase at a distance between 3×10^3 and 2×10^4 au from the centre. The differences between the two approaches are likely related to the use of a more realistic energy deposition by the cascade particles, which is included in the GEANT4 Monte Carlo toolkit calculations.

As discussed in Paper I, the temperature increase caused by the CRs within the MC also affects the chemical balance, as it allows some reaction pathways to proceed more efficiently in specific layers inside the cloud. Such processes are of great importance in astrochemistry and astrobiology. Future work will address the effects of the interstellar magnetic field, as well as the effects of the mass and density law within the MC.

3.3 Behaviour of the molecular reaction rates within the cloud

In this section, we discuss, in qualitative terms, the behaviour of selected reaction-rate constants (normalized values) within the MC that, in some sense, are affected directly or indirectly by the CR

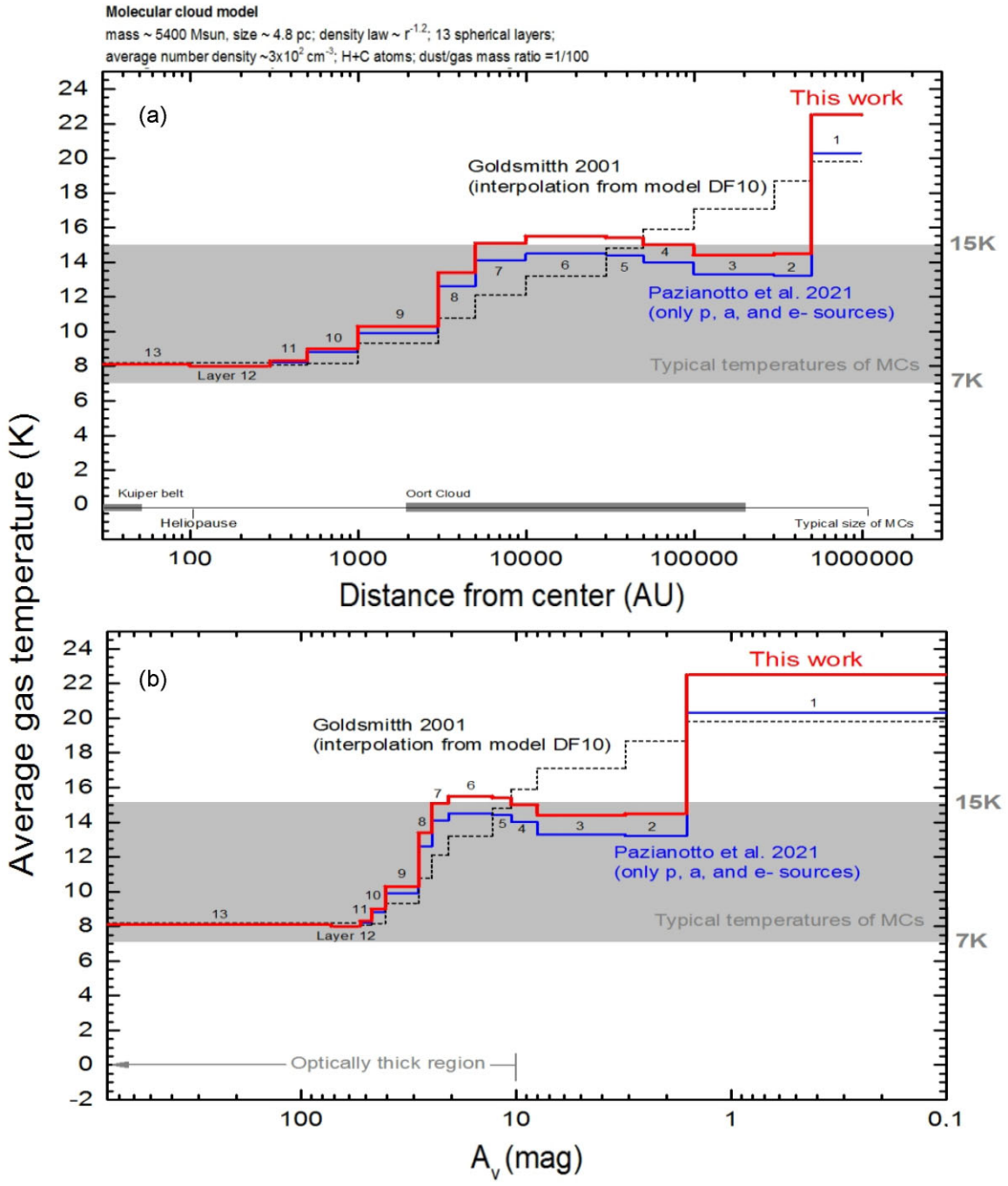

Figure 6. Molecular cloud temperature profile (gas temperature) of each modelled layer, exposed to a realistic CR field (containing light particles, medium-mass ions, and heavy ions) and considering the thermal balance in a steady-state scenario. The red line is the estimate using the current CR energy input, the blue line is the calculation using only light particles (from Paper I), and the dashed black line is the calculation from Goldsmith (2001) (model DF). (a,b) The cloud´s temperature as a function of the central distance and the average visual extinction, respectively. The figure header indicates some parameters of the current model.

energy input. It is worth noting that the velocity rate of a given molecular reaction can be obtained by multiplying the reaction-rate constant by the number density of the given molecular or atomic species considered. Good reviews on the type of chemical reactions and the reaction rates applied to space environments can be obtained in Wakelam et al. (2010, 2012).

Here, we consider that the reaction-rate constant for CR-induced ionization can be written as $k_{CR} \propto n(H_2)^{-0.5} \sim A_v{}^{-0.5}$, following the empirical assumption of CRs in dense interstellar clouds (Caselli 2003; Yeghikyan 2011) and the relation between the molecular column density and the visual extinction (Bohlin, Savage & Drake 1978). Additionally, as discussed by Wakelam et al. (2010, 2012), the bimolecular reaction-rate constant and the ion-neutral reaction-rate constant in cold space environments, as a good approximation, can be described by $k_{A+B} \propto T \times e^{-T}$and $k_A+_{+B} \propto T^{-0.5}$, respectively. The reaction-rate constant due to the photoionization process, mostly

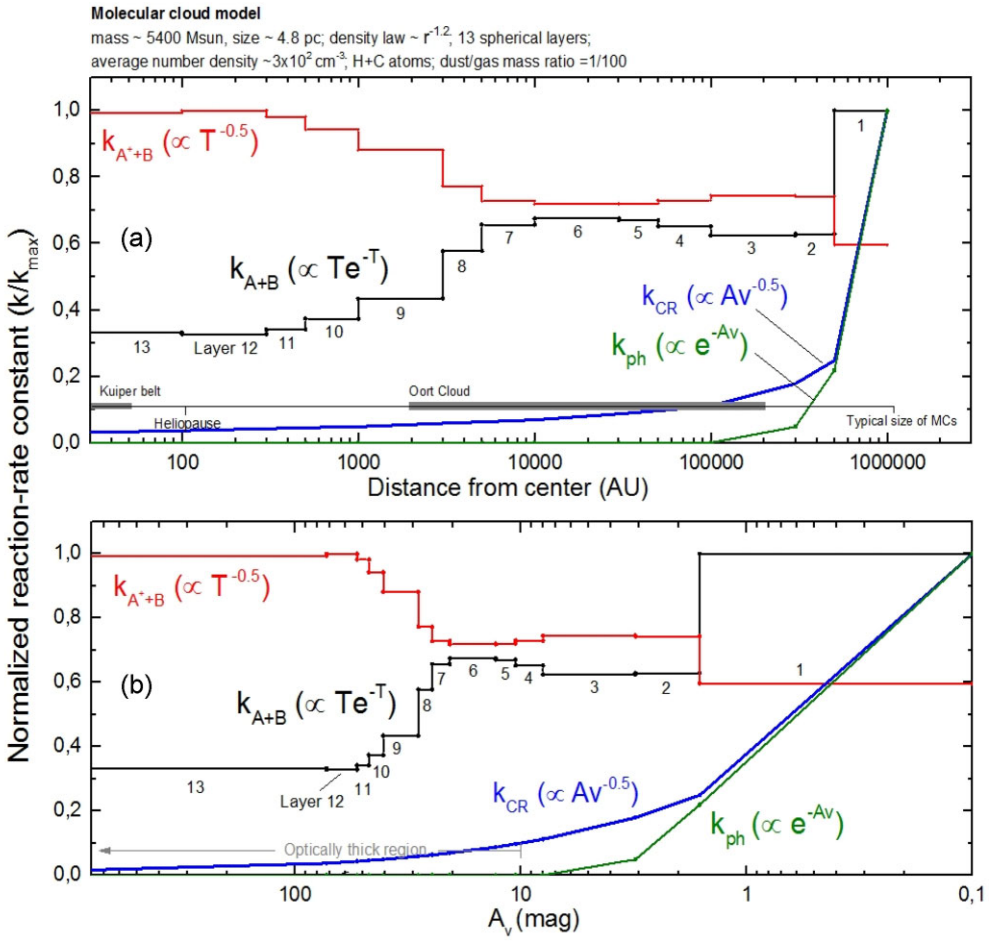

Figure 7. The evolution of the selected normalized reaction-rate constant within the MC in the presence of the incoming realistic CR field. The presented reaction-rate constants are for the photoionization (k_{ph}), CR-induced ionization (k_{CR}), bimolecular reactions (k_{A+B}), and ion-neutral reactions (k_{A++B}). The numbers of the layers in the model are indicated by the black labels. The presented values were calculated at the inner radius of each layer, and the lines are only to guide the eyes. Some model parameters are given in the figure header.

by UV, follows the attention Lambert–Beer law, which allows us to consider that $k_{ph} \propto e^{-A_v}$ within the cloud. It is worth noting that the reaction-rate constant for the dissociation processes, triggered by either photons or CRs, should also follow the same behaviour as the respective reaction-rate constant for the ionization.

Fig. 7 presents the selected normalized reaction-rate constants (k_{CR}, k_{ph}, k_{A+B}, and k_{A++B}) as a function of distance to the centre of the cloud (panel a) and as a function of the visual extinction within the cloud (panel b). The ionization reaction rates triggered by both UV photons and CRs decrease very fast to the central regions due to the enhancement of visual extinction. However, due to the exponential dependence of k_{ph} on A_v, k_{ph} decreases much faster than k_{CR} as the distance to the centre of the cloud decreases, indicating, once more, that CRs are mainly responsible for triggering ionization (and also dissociation) processes in the obscured regions of the cloud. However, as pointed out by Caselli (2003), a decrease of the CR ionization rate towards the inner part of the cloud does not affect the thermal balance of the dense core as long as gas and dust are well coupled.

Another interesting feature observed in Fig. 7 is that, with the exception of the outer layer of the cloud, the bimolecular reaction-rate constant has a maximum at the sixth layer, around 1–3 $\times$ 10^4 au (A_v ~15–20 mag), which could suggest that molecular formation could be enhanced in such regions, due to the small bump in temperature induced by the CRs. Curiously, due to its peculiar dependence on the temperature, the ion-neutral reaction-rate constant has a maximum in the deep core and decreases to the outer layers of the cloud.

4 CONCLUSIONS

This work presents in a more realistic way (considering a broad range of different incoming particles and their flux measured in the ISM) the energy delivered by CRs in a typical MC (mass ~5400 $M_\odot$ and size ~10^6 au; mainly of H, with a density law of $r^{-1.2}$ and average number density of ~300 cm^{-3}) considering the energy deposition of light particles (from Pazianotto et al. 2021), medium-mass ions (this work), and heavy ions (from Pilling et al. 2021). Simulations of the energy released by CR-induced particles were performed using the Monte Carlo code GEANT4, which takes into account nuclear physics and cascade particle processes. The CR flux measured by the *Voyager* spacecraft ISM was considered (taken from Cummings et al. 2016). Using a first-order approximation, it is possible to calculate the temperature gradient between the MC volumes using the deposited energy. The main conclusions are as follows:

(1) The carbon ion was considered as a representative constituent of the medium-mass group. We have determined the energy

deposition rate as a function of the centre of the MC for several kinds of cascade particles due to the interaction of carbon with clouds' matter. As expected, the carbon ions represent the most important component when the carbon source is considered, followed by secondary electrons, alphas, protons, deuterons, and others. The energy deposition of carbon and the secondary electrons has a maximum in the outer layers of the cloud. For the other particles, we observe the contrary behaviour (the maximum energy deposition occurs in the deep centre of the cloud). For all the sources considered, the secondary photons have the lowest gradient in the energy deposition of the cascade particles.

(2) In terms of integrated flux, the C ions are the dominant agent in this group, followed by O, B, and N ions. Curiously, in terms of the deposited energy inside the MC, the O ions are dominant, followed by C, Ne, and N. Within this medium-mass group, the F ions present the lowest value for both the integrated flux and the energy deposition rate.

(3) The results show that the incoming protons are indeed the dominant source in the energy deposition and heating, followed by alphas and electrons, with medium-mass ions and heavy ions contributing roughly 8 per cent to each group. The maximum value of the deposited energy rate was observed in the outer layer of the MC (436.9 MeV g^{-1} s^{-1}) and the minimum deposited energy occurred in the deep core of the cloud (151.9 MeV g^{-1} s^{-1}). Considering the radial energy deposition gradient as a whole, there was a small enhancement at a distance of around 1000 au from the centre.

(4) The current model also shows a temperature enhancement of up to 10 per cent in the cloud's outer layers (reaching up to 22.5 K) with respect to the previous calculations where only light particles are considered. However, in the deep core of the cloud, neither heavy nor medium-mass ions contribute to the temperature enhancement.

(5) The qualitative analysis of the bimolecular reaction-rate constant indicates that, with the exception of the outer layer of the cloud, it has a maximum around 1–3 $\times$ 10^4 au (A_v $\sim$15–20 mag), which could suggest that molecular formation could be enhanced in such regions, due to the small bump in temperature induced by the CRs. However, the ion-neutral reaction-rate constant has its maximum in the colder and central region.

The energy deposition rate due to CRs, which modulates the gas temperature profile within the MC, allows us to better constrain the reaction-rate constants of specific reactions and may help produce more realistic astrochemical models in the future.

ACKNOWLEDGEMENTS

SP acknowledges the Brazilian research agency CNPq (projects #306145/2015-4; #302985/2018-2). MTP thanks the São Paulo Research Foundation for the financial support (project #2019/13577-0), LAB-CCAM from ITA, and ENU-IEAv for computational support.

DATA AVAILABILITY

The data underlying this article will be shared on reasonable request to the corresponding author.

REFERENCES

Agostinelli S. et al., 2003, Nucl. Instrum. Methods Phys. Res. A, 506, 250
Allison J. et al., 2006, IEEE Trans. Nucl. Sci., 53, 270
Boduch P. et al., 2015, JPCS, 629, 012008
Bohlin R. C., Savage B. D., Drake J. F., 1978, ApJ, 224, 132
Caselli P., 2003, ApSS, 285, 619
Cummings A. C. et al., 2016, ApJ, 831, 18
de Barros A. L. F., da Silveira R. F., Pilling S., Domaracka A., Tothard H., Boduch P., 2014, MNRAS, 438, 2026
De Mendonça R. R. S. et al., 2013, J. Geophys. Res. Space Phys., 118, 1403
Dobbs L. C. et al., 2014, in Bleuther H., Klessen R. S., Dullemond C. P., Henning T., eds, Protostars and Planets VI. Univ. Arizona Press, Tucson, AZ, p. 3
Fredon A., Radchenko A. K., Cuppen H. M., 2021, Acc. Chem. Res., 54, 745
Galli D., Padovani M., 2015, Proc. Sci., 221, 019
GEANT4 Collaboration, 2012, GEANT4 Physics Reference Manual v9.6, https://geant4-userdoc.web.cern.ch/UsersGuides/PhysicsReferenceManual/BackupVersions/V9.6/fo/PhysicsReferenceManual.pdf
Goldsmith P. F., 2001, ApJ, 557, 736
Goldsmith P. F., Langer W. D., 1978, ApJ, 222, 881
Grassi T., Padovani M., Ramsey J. P., Galli D., Vaytet N., Ercolano B., Haugbølle T., 2019, MNRAS, 484, 161
Grudić M. Y., Hopkins P. F., Lee E. J., Murray N., Faucher-Giguère C.-A., Johnson C. L., 2019, MNRAS, 488, 1501
Hopkins P. F. et al., 2020, MNRAS, 492, 3465
Loewenstein M., Zweibel E. G., Begelman M. C., 1991, ApJ, 377, 392
Ly X. Y. et al., 2012, A&A, 546, A81
Pan L., Padoan P., 2009, ApJ, 692, 594
Pazianotto M. T., Pilling S., Quesada Molina J. M., Federico C. A., 2021, ApJ, 911, 129(Paper I)
Pilling S., Seperuelo Duarte E., Domaracka A., Rothard H., Boduch P., da Silveira E. F., 2011, Phys. Chem. Chem. Phys., 13, 15755
Pilling S., Andrade D. P. P., da Silveira E. F., Rothard H., Domaracka A., Boduch P., 2012, MNRAS, 423, 2209
Pilling S., Pazianotto M. T., de Souza L. A., 2021, ApJ, 921, 116(Paper II)
Rachid M. G. et al., 2020, MNRAS, 494, 2396
Savić M. et al., 2019, Astropart. Phys., 109, 1
Vasconcelos F. A., Pilling S., Rocha W. R. M., Rothard H., Boduch P., 2017a, Phys. Chem. Chem. Phys., 19, 24154
Vasconcelos F. A., Pilling S., Rocha W. R. M., Rothard H., Boduch P., 2017b, ApJ, 850, 174
Vasconcelos F. A., Pilling S., Rocha W. R. M., Rothard H., Boduch P., Ding J. J., 2017c, Phys. Chem. Chem. Phys., 19, 12845
Wakelam V. et al., 2010, Space Sci. Rev., 156, 13
Wakelam V. et al., 2012, ApJS, 199, 21
Yeghikyan A. G., 2011, Int. Schol. Res. Notices, 2011, 905015

This paper has been typeset from a TEX/LATEX file prepared by the author.